

Oscillation quenching in Stuart-Landau oscillators via dissimilar repulsive coupling

Subhasanket Dutta¹, Omar Alamoudi^{2,4}, Yash Shashank Vakilna², Sandipan Pati^{2,*} and Sarika Jalan^{1,3,†}

¹Complex Systems Lab, Department of Physics, Indian Institute of Technology Indore, Khandwa Road, Simrol, Indore-453552, India

²Texas Institute for Restorative Neurotechnologies, The University of Texas Health Science Center at Houston, Houston, Texas 77225, USA

³Department of Biosciences and Biomedical Engineering, Indian Institute of Technology Indore, Khandwa Road, Simrol, Indore-453552, India

⁴Biomedical Engineering Program, King Abdulaziz University, Jeddah, Saudi Arabia



(Received 26 June 2022; accepted 4 November 2022; published 2 February 2023)

Quenching of oscillations, namely, amplitude and oscillations death, is an emerging phenomenon exhibited by many real-world complex systems. Here, we introduce a scheme that combines dissimilar couplings and repulsive feedback links for the interactions of Stuart-Landau oscillators and analytically derive the conditions required for the amplitude death. Importantly, this analysis is independent of the network size, presents a generalized approach to calculate the stability conditions for various different coupling schemes, and befits nonidentical oscillators as well. Last, we discuss the similarities of the quenching of oscillations phenomenon with the postictal generalized Electroencephalogram (EEG) suppression in convulsive seizures.

DOI: [10.1103/PhysRevResearch.5.013074](https://doi.org/10.1103/PhysRevResearch.5.013074)

I. INTRODUCTION

Coupled Stuart-Landau (SL) oscillators can display a wide range of emerging phenomena, such as synchronization, pattern formation, quenching of oscillations, etc. In particular, quenching of oscillations arising due to coupling between the pairs of oscillators has drawn considerable attention from the nonlinear dynamics community due to the widespread occurrence of this phenomenon in many natural systems. For example, in laser systems, various types of couplings among the laser components can lead to the quenching of oscillation [1]. In neurological systems, oscillation death has been proposed to be the root cause of various neurodegenerative diseases and has been modeled using coupled nonlinear oscillators [2]. A few other systems manifesting quenching of oscillations are atmosphere [3], electronic circuits [4], etc.

There have been persistent efforts to realize the quenching of oscillations in various nonlinear model systems, among which coupled Stuart-Landau oscillators turn out to be apt for understanding the origin and implications of such behaviors. Quenching of oscillations in coupled Stuart-Landau oscillators are primarily achieved in three manners, by introducing a parameter mismatch [5], communication delays [6], and conjugate coupling [7]. Few experimental setups incorporating these designs have successfully achieved oscillations quenching or the death state [8]. A death state of an oscillator can

be classified into two major categories: amplitude death (AD) and oscillation death (OD). Amplitude death corresponds to all the oscillators settling down to the same fixed point located at the origin. In oscillation death, oscillators settle at different fixed points or the same fixed point away from the origin [6] (Fig. 1). The dynamical equation for an uncoupled SL oscillator can be written by

$$\dot{z}(t) = (a^2 - |z(t)|^2)z + i\omega z. \quad (1)$$

Here z is a complex variable depicting the dynamical state of an oscillator with ω being its intrinsic frequency. The oscillator has one unstable fixed point acting as a center for a stable circular limit cycle of radius a .

A set of identical SL oscillators ($\omega_i = \omega_j$) is unable to show quenching of oscillation with a simple diffusive coupling through the z variable. However, different coupling schemes play different governing roles in determining steady-state behaviors. For instance, the oscillation death state is achieved for the coupling term being present only in the real or

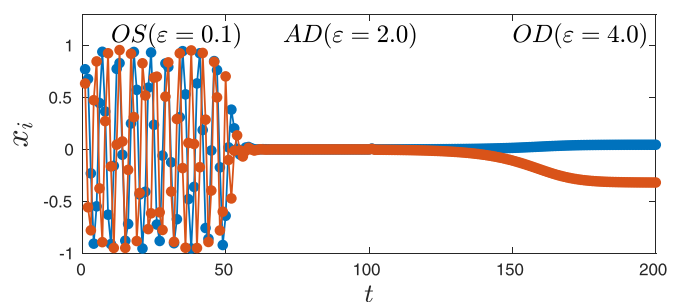


FIG. 1. x_i vs t plot depicting three different dynamical states for two randomly selected nodes from a network of $N = 1000$ [Eq. (3)]. Lorentzian frequency distribution parameters are $\omega_0 = 2.0$ and $\Delta = 0.30$.

*patilabuab@gmail.com

†Corresponding author: sarika@iiti.ac.in

imaginary part of z [5]. In fact, there could be a transition from the oscillatory state (OS) to AD when z is coupled diffusively with its conjugate z^* [7]. Moreover, in the identical oscillators, repulsive feedback coupling [9,10] and diffusive coupling in dissimilar (also referred to as conjugate) variables [2,11] can steer AD and OD. In nonidentical oscillators, frequency mismatch and coupling strength are enough to bring the oscillator death, even for simple diffusive coupling via the z variable. Nonidentical SL oscillators coupled through diffusive couplings on small-world networks have been shown to support OD [12,13], and on scale-free networks have been shown to yield a complete AD state [14]. Lately, the first-order abrupt transition to AD, popularly referred to as explosive death, has become a topic of great interest due to the theoretical curiosity fueled by observations of the phenomenon's existence in many real-world systems. The first-order transition to AD can be successfully induced in coupled oscillators via an environmental coupling scheme in a single layer [15,16] as well as in multiplex networks [17,18].

Further, there have been persistent efforts to model large-scale brain networks using coupled oscillators on networks [19–22]. For example, few previous studies have considered simple linear phase oscillators to understand various emerging dynamical features of brain networks [19]. A simple brain network model consists of firing neurons acting as nodes connected through synapses defining interactions between the pairs of neurons. Dynamical behaviors of an individual neuron/node were first studied by the Hodgkin-Huxley model, explaining the initiation and propagation of action potential in neurons [23]. Subsequently, other models like Fitzhugh-Nagumo (explaining spiking in neurons) and Hindmarsh-Rose (explaining spiking, bursting in neurons) [24,25] were discovered. However, in large-scale brain networks, the collective behavior of the nodes was considered to be quite low dimensional, and information about the dynamical evolution of each neuron was shown to be relatively irrelevant [26,27]. A well-known model representing large-scale brain dynamics is the neuronal mass model, which presents an ensemble approach in which the dynamics of a patch of the cortex (a local population of neurons) are represented by a set of differential equations reduced in dimension [26]. Further advances in this field led to the discovery of more realistic models, such as the whole brain model and the brain networks model, where brain areas were treated as nodes in a coupled dynamical system. These patches of the cortex are considered as units or nodes coupled with each other according to their anatomical connectivity (edge) patterns. Simplified models such as the Kuramoto oscillator [28] and SL oscillators [22,29,30] have been used in a similar fashion to portray large-scale brain dynamics. Different models are constructed such that they can explain the phenomenon of interest [27,28].

Synchronized activities among the different brain regions have been associated with the onset of the seizure from the pre-seizure region [19]. It is common knowledge that soon after the generalized tonic-clonic seizures, the brain state exhibits a transition to an isoelectric EEG state, with the existence of a profound scalp EEG voltage attenuation ($< 10 \mu\text{V}$), referred to as the postictal generalized EEG suppression (PGES) [20,21]. While we do not claim that the model

presented here provides a mechanism behind the occurrence of PGES in the human brain, the phenomenon depicted by this model bears a close resemblance to PGES. Furthermore, to make the modeling of PGES more realistic, for the coupling matrix of Eq. (3), we have considered the functional correlation matrices generated for the EEG time series data from brain during seizure.

First, we develop a theoretical framework to analyze amplitude death in coupled SL oscillators on complex networks. Earlier theoretical works on SL oscillators pertain to the linear stability analysis for direct mean-field diffusive coupling [31] and diffusive conjugate coupling [7] on globally coupled and star networks [32]. We consider SL oscillators with dissimilar repulsive feedback couplings and develop an analytical approach that is independent of the size of the underlying coupling network. The method is a generalized one as it facilitates calculations of necessary and sufficient conditions to attain amplitude death for other coupling forms. The key lies in the fact that the analysis uses a generalized form of coupling matrix, providing it an edge over previously existing frameworks. Then, we numerically study the dynamical behaviors of this setup on various network architectures, namely, globally coupled networks, regular lattice networks, Erdős-Rényi (ER) random networks. Finally, we numerically analyze the results of Eq. (1) with the functional coupling matrices generated from real time series EEG data of patients, and discuss the similarity between the phenomenon depicted by the model with PGES.

II. MODEL

Dynamical evolution of an uncoupled SL oscillator is governed by Eq. (1). Upon substituting $z = x + iy$, the resulting equation is

$$\dot{x}_k = P_k^x, \quad \dot{y}_k = P_k^y, \quad (2)$$

where

$$P_k^x = (1 - x_k^2 - y_k^2)x_k - w_k x_k, \\ P_k^y = (1 - x_k^2 - y_k^2)y_k + w_k y_k.$$

An introduction of the dissimilar repulsive feedback coupling between a pair of connected nodes through both the x and y coordinates results in the following equation:

$$\dot{x}_k = P_k^x - \frac{\epsilon_x}{N} \sum_{j=1}^N A_{jk}(y_j + x_k), \\ \dot{y}_k = P_k^y - \frac{\epsilon_y}{N} \sum_{j=1}^N A_{jk}(x_j + y_k). \quad (3)$$

Here A_{jk} is the adjacency matrix representing the underlying network structure. For an unweighted network, its elements take the value 1 when j th and k th nodes are connected, and 0 otherwise. Whereas, for a weighted network, the elements of the adjacency matrix are represented by the interaction weights. For identical oscillators, it has been found that an introduction of the similar diffusive coupling does not yield oscillator death (see Appendix A 1), whereas dissimilar repulsive feedback links bring oscillator death. Further,

TABLE I. Amplitude (A) and oscillation (E) death measures for different states.

Name	A	E
AD	$= 0$	$= 0$
OD	$= 0$	$\neq 0$
OS	$\neq 0$	$\neq 0$

we consider different cases with the nodes having different coupling schemes and couplings being in only one dimension. We consider the weighted interaction matrix generated from the postseizure data. First, we model the eight intracranial channels of the brain as nonidentical Stuart-Landau oscillators on a directed weighted network. The dynamical equation of such nodes can be given by Eq. (3) with ω chosen from a Lorentzian frequency distribution with parameters corresponding to the frequency band. Further, we study the dynamics of each node and the network as a whole.

Coupling of a SL oscillator with another SL oscillator may either give birth to additional fixed points than those that exist for the single uncoupled oscillator, or may change the stability properties of the existing fixed point(s). In the following we define an order parameter which quantifies the variance of fluctuation of the dynamical variables over a time span, which tends to 0 for both OD and AD cases:

$$r = \frac{1}{N} \sum_{i=1}^N ((x_i)_{\max,t} - (x_i)_{\min,t}), \quad E = \frac{\sum_{i=1}^N |z_i|^2}{N}.$$

For numerical purposes, if $0 < E < 0.001$ and $0 < r < 0.001$, we infer that the system has reached the state of AD (Table I).

Further, the different network architectures to define pairwise interaction matrices are constructed as follows. In a regular one-dimensional (1D) ring lattice, each node is connected to its k neighbors. To produce an ER random network with an average degree n/N , we randomly connect n edges out of the possible $N(N - 1)/2$ edges [33]. The scale-free network here is created via the Barabasi-Albert model in the following manner: starting with an initial m_o number of nodes, at each time step, one node with m connections ($m < m_o$) is added. The connection probability of this new node getting attached to an existing node is proportional to the degree of that node.

III. ANALYTICAL CALCULATION

Let us now provide the mathematical formalism to analyze the stability of coupled SL oscillators on various setups. First, we present the generalized characteristic equation for the coupled SL oscillators on globally coupled networks. Thereafter, we consider globally coupled nodes having dissimilar repulsive feedback couplings and try to solve using the generalized characteristics equation. We further mix various kinds of couplings and study the dynamical evolution of the coupled oscillators for the mixed setup.

At first, let us consider a setup of globally coupled SL oscillators with a generalized form of the coupling matrix F , which can be changed later according to the different setups.

The generalized coupled differential equations for globally coupled networks of the Stuart-Landau oscillators can be written as

$$\begin{bmatrix} \dot{x}_k \\ \dot{y}_k \end{bmatrix} = \begin{bmatrix} (1 - x_k^2 - y_k^2)x_k - i\omega_k y_k \\ (1 - x_k^2 - y_k^2)x_k - i\omega_k y_k \end{bmatrix} + F(x_j, x_k, y_j, y_k).$$

The corresponding Jacobian matrix takes the form

$$|I\lambda - M| = \begin{pmatrix} M_1 + F_1 & \cdot & \cdot & F_1 \\ F_2 & M_2 + F_2 & \cdot & \cdot \\ F_i & \cdot & M_i + F_i & \cdot \\ F_N & \cdot & \cdot & M_N + F_N \end{pmatrix},$$

where $M_i = \begin{pmatrix} \lambda - a_1 & -\omega_i \\ \omega_i & \lambda - a_2 \end{pmatrix}$. However, a_1 , a_2 , and F_i vary in accord with the coupling scheme of each node. To deduce the stability conditions for the AD state, the challenge lies in solving the characteristic equation for the corresponding Jacobian matrix (M) given by $\det(I_{2N}\lambda - M) = 0$. Let us first solve $\det(I_{2N}\lambda - M) = 0$, for which we use the following lemma.

Matrix-determinant lemma. If X is $n \times n$, and U and V are $n \times m$ matrices,

$$|X + UV^T| = |X| \times |I_m + V^T X^{-1} U|, \quad (4)$$

where I_m is an identity matrix of the dimension $m \times m$ and $O_{n \times n}$ is a null matrix of dimension $n \times n$.

Proof. To prove this theorem we will expand the determinant as follows: ■

$$|X + UV^T| = \begin{vmatrix} X + UV^T & U \\ O_{n \times n} & I_m \end{vmatrix} \begin{vmatrix} I_n & O_{n \times m} \\ -V^T & I_m \end{vmatrix} = \begin{vmatrix} X & U \\ -V^T & I_m \end{vmatrix},$$

$$\begin{vmatrix} X & U \\ -V^T & I_m \end{vmatrix} = |X| \times |I_2 + V^T X^{-1} U|$$

using identity for the determinant of block matrices,

$$\begin{vmatrix} A & B \\ C & D \end{vmatrix} = |D| \times |D - CA^{-1}B|. \quad (5)$$

Next, we apply the following lemma to find out the characteristic equation and the corresponding eigenvalues. ($\lambda I_{2N} - M$) can be written as

$$(\lambda I_{2N} - M) = M_d + UV^T,$$

where

$$M_d = \begin{bmatrix} M_1 & 0 & 0 & \cdot & \cdot & \cdot \\ 0 & M_2 & 0 & 0 & \cdot & \cdot \\ \cdot & \cdot & \cdot & \cdot & \cdot & \cdot \\ \cdot & \cdot & \cdot & \cdot & \cdot & \cdot \\ 0 & 0 & \cdot & \cdot & \cdot & M_N \end{bmatrix},$$

$$U = \begin{bmatrix} F_1 \\ F_2 \\ F_3 \\ \cdot \\ \cdot \end{bmatrix}, \quad V = \begin{bmatrix} I_2 \\ I_2 \\ \cdot \\ \cdot \end{bmatrix}.$$

By using the matrix determinant lemma [Eq. (4)] and Eq. (5) we obtain

$$\begin{aligned} |\lambda I_{N/2} - M| &= |M_d| \times |I_2 + V^T M_d^{-1} U| \\ &= |M_d| \times \left| I_2 + V^T \left(\frac{\text{adj}(M_d)}{|M_d|} \right) U \right| \\ &= \prod_{i=1}^N |M_i| \times \left| I_2 + \sum_{i=1}^N \frac{\text{adj}(M_i) F_i}{|M_i|} \right|. \end{aligned}$$

The generalized characteristic equations are given by

$$\prod_{i=1}^N |M_i| = 0 \quad \text{and} \quad \left| I_2 + \sum_{i=1}^N \frac{\text{adj}(M_i) F_i}{|M_i|} \right| = 0, \quad (6)$$

where $\text{adj}(M_i)$ is the adjoint matrix of M_i . What follows is that the characteristic equation reduces to a determinant of a 2×2 matrix which is independent of the size of the network. Moreover, such a reduction allows this scheme to work even when nodes are connected through a different form of the coupling provided each node has the same coupling scheme separately. Let us consider various different cases as test beds for the analysis. Note that the simplest case is the one where identical oscillators are diffusively coupled. This coupling does not exhibit AD Appendix A 1.

a. Introduction of dissimilar repulsive feedback coupling. First, we consider a system where all nodes are coupled via dissimilar repulsive feedback. The matrices M_i and F_i which remain the same for all values of i , can be given by $M_i = \begin{pmatrix} \lambda^{-1+\varepsilon} & \omega \\ -\omega & \lambda-1+\varepsilon \end{pmatrix}$ and $F_i = \begin{pmatrix} 0 & \varepsilon/N \\ \varepsilon/N & 0 \end{pmatrix}$. This setup yields the following eigenvalues:

$$\lambda = 1 - \varepsilon \pm \sqrt{\varepsilon^2 - \omega^2}, \quad \lambda = 1 - \varepsilon \pm i\omega. \quad (7)$$

The conditions for the origin to be a stable state is satisfied for $\text{Re}[\lambda_i] < 0$ for all i . Applying this condition, from Eq. (7) we get that for (i) $\varepsilon < \omega$, $\varepsilon > 1$, and (ii) $\varepsilon > \omega$, $1 - \varepsilon \pm \sqrt{\varepsilon^2 - \omega^2} < 0$ yielding $\varepsilon < (1 + \omega^2)/2$.

Now we consider a system of identical oscillators with two kinds of coupling. Some nodes have coupled via repulsive dissimilar coupling, whereas others have coupled via simple diffusive coupling. The dynamical equation for the simple diffusively coupled nodes can be given by Eq. (A1) of Appendix A 1, whereas the nodes with the repulsive link will be governed by Eq. (3). Proceeding similarly to the last section, the coupling matrices for the nonrepulsive and the repulsive schemes are given by F_1 and F_2 , respectively. However, the matrices M_1 and M_2 remain the same for both types of nodes. The M_1 , F_1 , and F_2 matrices are given by $M_1 = \begin{pmatrix} \lambda^{-1+\varepsilon} & \omega \\ -\omega & \lambda-1+\varepsilon \end{pmatrix}$, $F_1 = \begin{pmatrix} -\varepsilon/N & 0 \\ 0 & -\varepsilon/N \end{pmatrix}$, and $F_2 = \begin{pmatrix} 0 & \varepsilon/N \\ \varepsilon/N & 0 \end{pmatrix}$.

Next, if we consider a fraction of n nodes coupled with other nodes through the repulsive feedback couplings and a fraction of $1 - n$ nodes coupled without the repulsive links (referred to as the regular nodes), for a globally coupled network, the coupling matrix for the regular nodes will be given by F_2 and the coupling matrix corresponding to the repulsive nodes will be given by F_1 . Substituting them in Eq. (6) leads to the following eigenvalues:

$$\lambda_{1,2} = 1 - \varepsilon n \pm \sqrt{\varepsilon^2 n^2 - \omega^2}, \quad \lambda_{3,4} = 1 - \varepsilon \pm i\omega. \quad (8)$$

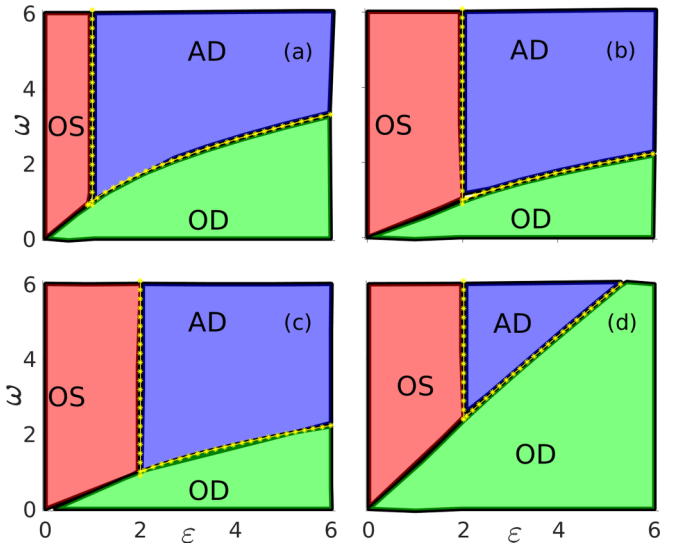


FIG. 2. Parameter space plot ω vs ε for a globally coupled network of size $N = 1000$ consisting of identical oscillators ($\omega_i = \omega_j = \omega \forall i, j$). (a) All nodes having dissimilar repulsive feedback coupling, (b) with half of the nodes having dissimilar repulsive feedback and another half with direct diffusive couplings, (c) dissimilar repulsive feedback coupling via x variable only, and (d) dissimilar repulsive feedback coupling via y variable only. The solid black lines represent the transition boundaries calculated numerically, whereas the yellow line represents the analytical region corresponding to the stable origin (AD).

The real part of these eigenvalues [Eq. (8)] must be negative for the amplitude death state to occur, which provides us the conditions $n > 1/\varepsilon$ and $\varepsilon < (1 + \omega^2)/2n$. Figures 2(a) and 2(b) confirm a perfect match between the numerical results and theoretical predictions for both the cases.

b. Dissimilar repulsive coupling in x variable. For the dissimilar repulsive coupling applied only to the x variable, the dynamics of the corresponding coupled equation will be governed by $\dot{x}_k = P_k^x - \frac{\varepsilon}{N} \sum_{j=1}^N (y_j + x_k)$, $\dot{y}_k = P_k^y$. The parameter space diagram obtained through the numerical calculations consists of AD and OS regions only. We find the necessary condition for these states to occur using the expression derived in Eq. (6). The matrices required for the calculation are $M = \begin{pmatrix} \lambda^{-1+\varepsilon} & \omega \\ -\omega & \lambda-1+\varepsilon \end{pmatrix}$ and $F = \begin{pmatrix} 0 & \varepsilon/N \\ 0 & 0 \end{pmatrix}$. Substituting them in Eq. (6) and solving this equation we get the following eigenvalues:

$$\begin{aligned} \lambda_{1,2} &= \frac{2 - \varepsilon \pm \sqrt{\varepsilon^2 - 4\omega^2 - 4\omega\varepsilon}}{2}, \\ \lambda_{3,4} &= \frac{2 - \varepsilon \pm \sqrt{\varepsilon^2 - 4\omega^2}}{2}. \end{aligned} \quad (9)$$

The necessary conditions can be derived from $\text{Re}[\lambda_{1,2} < 0]$ [Eq. (9)] as $\varepsilon > 2$ and $\varepsilon < (1 + \omega^2)/(1 - \omega)$ while $\varepsilon^2 - 4\omega^2 - 4\omega\varepsilon > 0$. From $\text{Re}[\lambda_{3,4} < 0]$ [Eq. (9)], one gets the necessary conditions as $\varepsilon > 2$ and $\varepsilon > 1 + \omega^2$. However, the condition $2 < \varepsilon < 1 + \omega^2$ prevails. This theoretical result matches with the numerical predictions illustrated in Fig. 2(c).

c. Dissimilar repulsive coupling through the y variable. Upon applying the dissimilar repulsive coupling in only

the y variable, the dynamical equation could be written as

$$\dot{x}_k = P_k^x, \quad \dot{y}_k = P_k^y - \frac{\varepsilon}{N} \sum_{j=1}^N (x_j + y_k).$$

Again using the same procedure as in the last section, we analytically confirm a match with the numerical results. Here, $M = \begin{pmatrix} \lambda - 1 & \omega \\ -\omega & \lambda - 1 + \varepsilon \end{pmatrix}$ and $F = \begin{pmatrix} 0 & 0 \\ \varepsilon/N & 0 \end{pmatrix}$.

Solving the generalized characteristic equation for these M and F values yields the following eigenvalues:

$$\lambda_{1,2} = \frac{2 - \varepsilon \pm \sqrt{\varepsilon^2 - 4\omega^2 + 4\omega\varepsilon}}{2},$$

$$\lambda_{3,4} = \frac{2 - \varepsilon \pm \sqrt{\varepsilon^2 - 4\omega^2}}{2}. \tag{10}$$

For the origin to be stable, we need $\text{Re}[\lambda] < 0$. Therefore, from $\text{Re}[\lambda_{1,2}] < 0$ [Eq. (10)] we derive the conditions $\varepsilon > 2$ and $\varepsilon < (1 + \omega^2)/(1 + \omega)$, and similarly $\text{Re}[\lambda_{3,4}] < 0$ [Eq. (10)] yields $\varepsilon > 2$ and $\varepsilon < (1 + \omega^2)$. The condition $\varepsilon < (1 + \omega^2)/(1 + \omega)$ is dominant and provides us the governing equation characterizing the transition between the AD and OD states, which also matches with the numerical results [Fig. 2(d)].

d. Nonidentical oscillators. Next, we consider the case of nonidentical oscillators, i.e., $\omega_i \neq \omega_j$. For Lorentzian intrinsic frequency distribution given by $g(\omega) = \frac{\Delta}{\pi[(\omega - \omega_0)^2 + \Delta^2]}$, one obtains the following characteristic equation:

$$\frac{1}{\varepsilon^2} = \left[\int_{-\infty}^{+\infty} \frac{\lambda - 1 + \varepsilon}{(\lambda - 1 + \varepsilon)^2 + (\omega)^2} g(\omega) d\omega \right]^2 + \left[\int_{-\infty}^{+\infty} \frac{\omega}{(\lambda - 1 + \varepsilon)^2 + (\omega)^2} g(\omega) d\omega \right]^2$$

which can further be written as $\frac{1}{\varepsilon^2} = \int_{-\infty}^{+\infty} \frac{1}{\lambda - 1 + \varepsilon + i\omega} g(\omega) d\omega \int_{-\infty}^{+\infty} \frac{1}{(\lambda - 1 + \varepsilon) - i(\omega)} g(\omega) d\omega$. The eigenvalues of this equation then can be given by

$$\lambda = 1 - \varepsilon + \Delta + \sqrt{\varepsilon^2 - \omega^2},$$

which yields the following condition for stability of the origin:

$$\text{If } \Delta > 1, \varepsilon > 1, \text{ and if } \Delta < 1, 1 < \varepsilon < \frac{(1 - \Delta)^2 + \omega_o^2}{2(1 - \Delta)}. \tag{11}$$

As seen from Fig. 3(b), the numerical results are in agreement with the analytical results [Eq. (11)]. The time series of two nodes for a system ($N = 1000$) with Lorentzian distribution ($\omega_o = 2.0$ and $\Delta = 0.33$) is shown in Fig. 1.

e. Bifurcation diagram. Figure 3(a) is drawn using XPPAUTO software [34] depicting two types of bifurcation. The first one is reverse Hopf bifurcation (HB) where a stable origin transforms into an unstable origin along with two stable limit cycles as the coupling strength decreases. The second one is pitchfork bifurcation (PB) where a stable origin becomes unstable and two more symmetric fixed points come into existence as coupling strength increases.

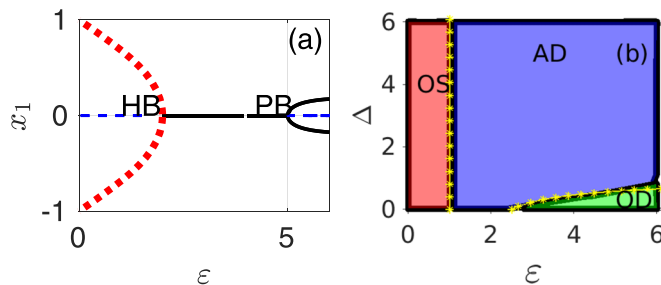


FIG. 3. (a) Bifurcation plot for dissimilar repulsive coupling via x variables for identical oscillators ($\omega = 2.0$); red dashed line corresponds to the stable limit cycle, solid black line represents the stable fixed point, and dashed black line represents an unstable limit cycle. (b) Parameter space Δ vs ε plot for nonidentical globally coupled networks of size $N = 1000$ and Lorentzian frequency distribution with $\omega_0 = 2.0$. The solid black and yellow dashed lines represent the transition boundaries calculated numerically and analytically, respectively.

IV. NUMERICAL RESULTS FOR VARIOUS MODEL NETWORKS

Next, we analyze the dynamical behaviors of coupled SL oscillators for this setup on various network architectures. We investigate how a particular network structure affects the onset of the oscillator death by considering four different network architectures apart from the globally coupled network, namely, the regular 1D lattice, ER random, small-world, and scale-free networks.

Among these, the scale-free and D lattices have the same lowest critical coupling strength at which AD occurs. While the small-world network has a slightly more critical coupling value as compared to the D lattice, the ER random network achieves AD at a higher critical coupling strength (Fig. 4). The above observation implicates that the critical coupling strength increases when the regular D lattice is distorted and changed to the ER random networks. Moreover, with an increase in the average degree of these, we observe a similar rise in the critical coupling network (as shown in Appendix A 2).

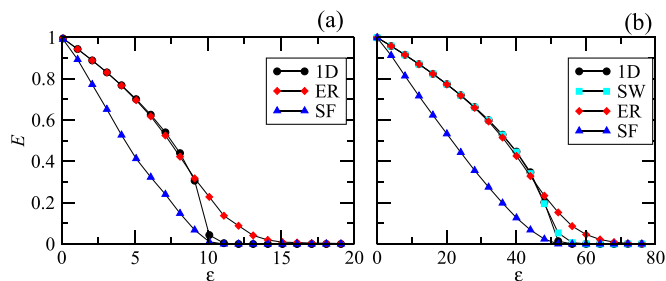


FIG. 4. E vs ε , for nonidentical oscillators with $\omega_0 = 5.0$ for various different network architectures (black circle, scale-free; red triangle, small world; blue square, regular; and green triangle, ER random networks). (a) $N = 100, \langle k \rangle = 10$. (b) $N = 1000, \langle k \rangle = 20$.

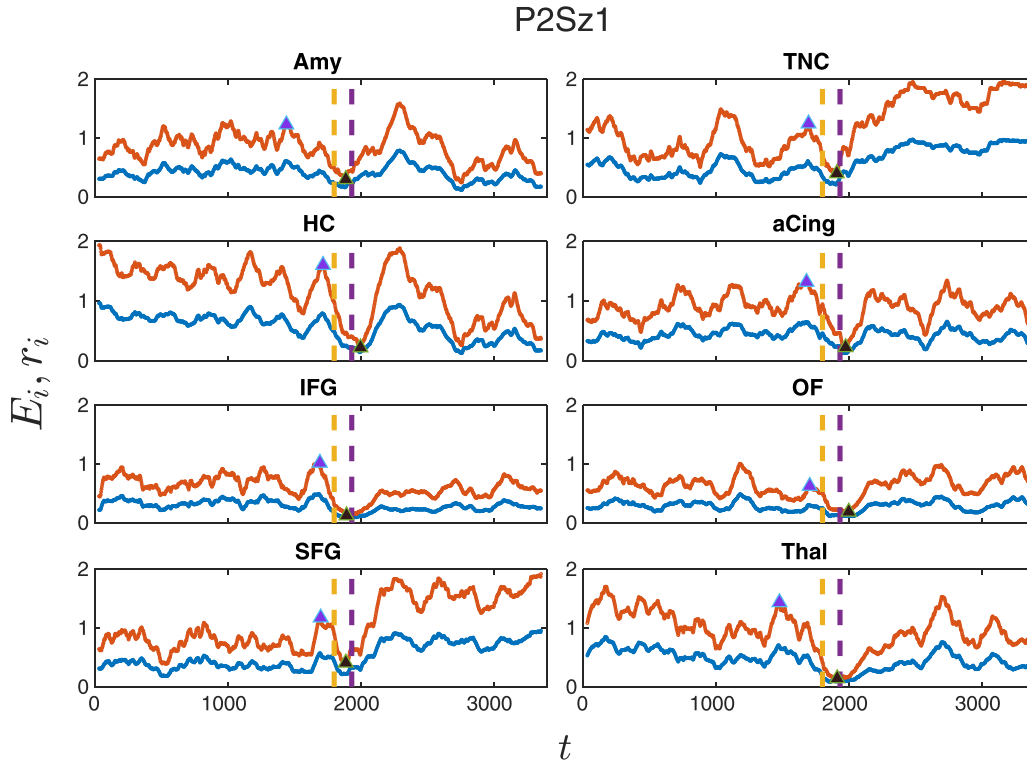


FIG. 5. Δ band for P2Sz1: The red and blue lines represent E_i vs t and r_i vs t , respectively. The yellow and violet dashed lines correspond to the start and end of the ictal region. Each subfigure represents the dynamics of a node (full names are provided in Appendix B).

V. SEIZURE DATA NETWORKS

PGES refers to the diffuse background attenuation (< 10 V) in the postictal state. The phenomenon is often observed following bilateral tonic-clonic seizures, and has been associated with a sudden unexpected death in epilepsy [35,36]. The mechanism and origin of occurrence of PGES are under intense investigations [37–39]. Here we show similarities of the phenomenon observed by Eq. (3) with PGES in convulsive seizures. We do not claim that Eq. (3) presents an accurate model to the brain activities; nevertheless, the quenching of oscillations manifested by the model bears a resemblance to PGES. Moreover, to bring the model a step closer to the brain activities, we present the results for the coupling architecture corresponding to the correlations matrices for the EEG multivariate time series data for seizure. This correlation matrix dataset consists of the $8 \times 8 \times f \times t$ tensor where f and t are, respectively, the number of the frequency levels and time steps for which data is recorded. The whole frequency range is divided into five bands or levels. The bands are as follows: Δ : 2–4; θ : 4–7; α : 8–12; β : 12–30; and γ : 30–40. Hence, each 8×8 matrix represents an adjacency matrix at a particular time at a particular frequency level. Each of these adjacency matrices is constructed by calculating the correlation between the time series of the eight channels at the corresponding frequency level for a particular time window. The detailed method for calculating Generalized Partial directed coherence (gPDC) matrices is given in Appendix B.

a. Overall oscillation suppression. While different regions for different patients reflect different behaviors, one typical pattern common in most of the nodes for all the patients is

that the amplitude starts to decrease in the ictal region as compared to the preictal region. Ergo, there exists a considerable suppression of the oscillation in the majority of the nodes around the ictal and in the initial stages of the postictal region for all the patients' data we have investigated. The amplitude remains low for the initial points of the postictal region and then slowly recovers with time (Figs. 5 and 6).

b. Mechanism of the amplitude death. The uncoupled equation represents a limit cycle oscillator, to which the coupling acts as a decaying term resulting in the amplitude death at certain values of the frequency and the coupling strength. The impact of this coupling term as a whole also depends on the associated coupling matrices (underlying network architectures), and therefore there exists a change in the critical coupling strength for which death occurs with the network structure. Additionally, the average degree of the network also plays a decisive role in deciding the amount of suppression of oscillations on the network.

VI. CONCLUSION

This paper proposes a coupling setup that yields oscillation death in coupled Stuart-Landau oscillators, and develops a theoretical framework to derive the necessary and sufficient conditions for attaining the oscillator death state for this setup with a fraction of nodes having repulsive feedback couplings. The analytical predictions are confirmed with the numerical experiments. Additionally, numerical results for the amplitude death on a few other model networks has been presented. Furthermore, we numerically analyzed the coupled dynamics model for the weighted correlations matrix constructed

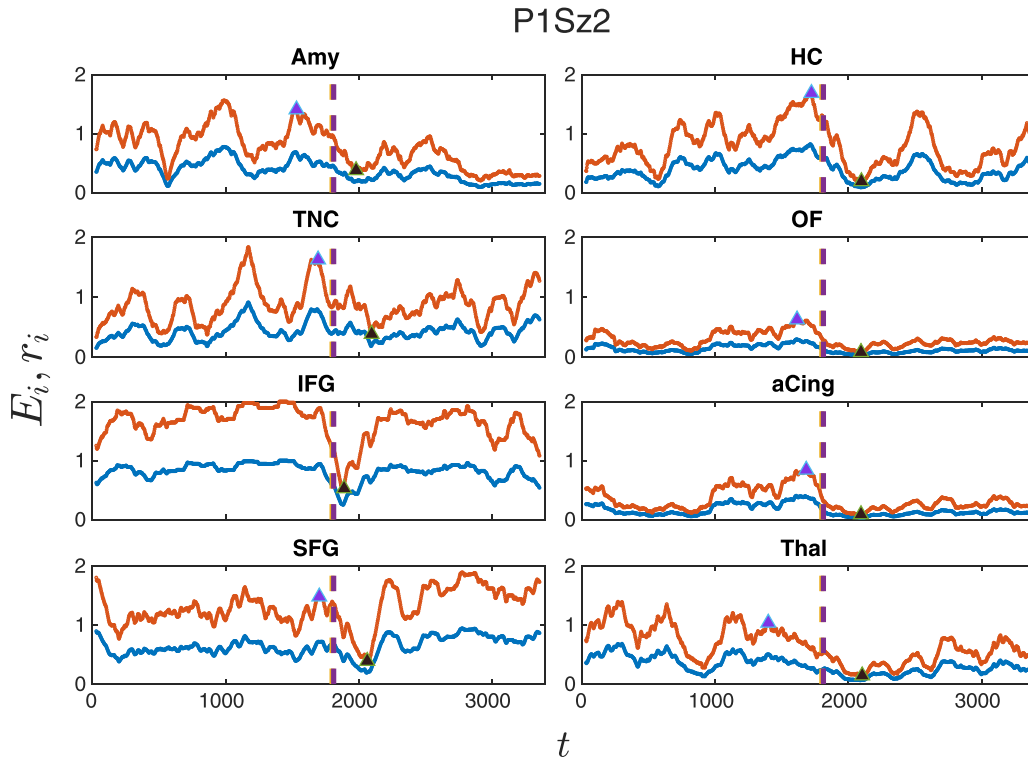


FIG. 6. Δ band for P1S2z: The red and blue lines represent E_i vs t and r_i vs t , respectively. The yellow and violet dashed lines correspond to the beginning and ending of the ictal region. Each subfigure represents the dynamics of a node (full names provided in Appendix B).

from the seizure data, and found that the phenomenon of amplitude suppression in the model resembles that with the PGES. One of the immediate future extensions of this work is to derive analytical conditions for other states than AD, and to develop a generalized theoretical framework that can incorporate various forms of the couplings [40] and adaptation rules [41,42]. Further future directions are to have a more realistic model for the brain and to replicate these results in a larger cohort, particularly by including a postictal state that lacks PGES to understand the origin of PGES. Furthermore, the neural underpinning of such OD to AD transition or oscillation suppression could also be harnessed towards developing neuromodulation therapy principled to perturbation of the coupling process to prevent or rescue OD/AD.

ACKNOWLEDGMENT

S.J. gratefully acknowledges DST POWER Grant No. SERB/F/9035/2021-2022.

APPENDIX A: EXTENSIONS ON THE MODEL

1. Oscillators without repulsive feedback coupling

An introduction of the diffusive coupling between a pair of connected nodes through both the x and the y coordinates results in the following equations:

$$\dot{x}_k = P_k^x + \frac{\varepsilon}{N} \sum_{j=1}^N A_{jk}(x_j - x_k), \quad \dot{y}_k = P_k^y + \frac{\varepsilon}{N} \sum_{j=1}^N A_{jk}(y_j - y_k). \tag{A1}$$

Here A_{jk} is the adjacency matrix representing the underlying network structure. For an unweighted network, its elements take the value 1 when the j th and k th nodes are connected, and 0 otherwise. Whereas, for a weighted network the elements of the adjacency matrix are represented by the interaction weights. Here, we consider the case of identical oscillators with all the nodes having the same frequency ω_0 . Next, we can proceed to calculate the Jacobian matrix and then F and M matrices. The coupling matrix F and matrix M for this model will be the following: $M = \begin{pmatrix} \lambda^{-1} + \varepsilon & -\omega_0 \\ \omega_0 & \lambda - 1 + \varepsilon \end{pmatrix}$ and $F = \begin{pmatrix} -\varepsilon/N & 0 \\ 0 & -\varepsilon/N \end{pmatrix}$. Next, by inserting them into Eq. (6), we get the solutions for the eigenvalues as

$$\lambda_{1,2} = (1 - \varepsilon) \pm i\omega,$$

$$\lambda_{3,4} = 1 \pm i\omega.$$

As we can see that one of these eigenvalues will always have a positive real part which can never be negative with the change in parameters, we can conclude that we can never obtain the amplitude death for this setup.

2. More on model networks

Here in Fig. 7 we have observed the dynamical behavior of nonidentical SL oscillators on ER random networks with the various average degrees. It was found that the critical value of coupling strength decreases as we increase the average degree of the ER random network.

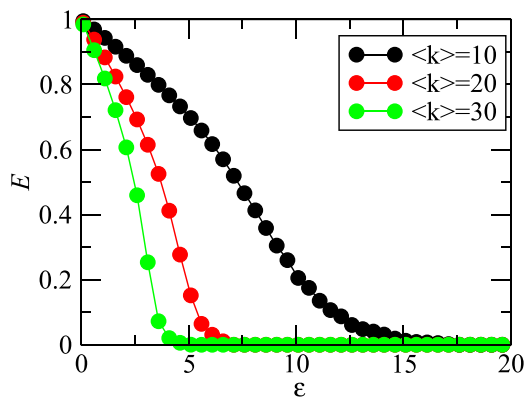


FIG. 7. E vs ϵ , for SL oscillators with dissimilar repulsive coupling on an ER random network with $N = 100$ with Lorentzian frequency distribution with $\omega_0 = 5.0$.

APPENDIX B: DATA GENERATION PROCESS

1. Patient and surgical procedure

Two adult patients with suspected drug-resistant temporal lobe epilepsy (mesial and temporal plus) underwent stereoelectroencephalography (SEEG) for localization of seizure foci. The Institutional Review Board approved the study for recording local field potentials (LFP) from the thalamus during SEEG exploration [43]. Before the surgery, the patients provided written consent for thalamic electrode implantation and recording for research purposes. The ethics, consenting process, safety, and accuracy of our thalamic implantation have been published previously [44]. The thalamic implanta-

tion was unilateral and ipsilateral to the seizure foci and none of the patients had any thalamic bleed or related neurological complications. Overall, four focal to bilateral tonic-clonic seizures (two seizures per patient) were analyzed.

2. Data acquisition

The optimal SEEG electrode implantation strategies were planned using robotic assistance (ROSA device; Medtech, Syracuse, NY) to sample thalamic nuclei and preplanned temporal network regions of interest. The multielectrodes (PMT Corporation, Chanhassen, MN) have 12–16 contacts per depth electrode, 2 mm contact length, 0.8 mm contact diameter, and 1.5 mm inter-contact distance. Natus Quantum (Natus Medical Incorporated, Pleasanton, CA; sampling rate 2048 Hz; hardware filters were present in the acquisition procedure: 0.08–13 Hz of sampling frequency hardware filtering; input noise 2 V peak to peak, and 16-bit precision) was used to record intracranial video EEG. Signals were referenced to a common extracranial electrode placed posteriorly in the occiput near the hairline.

3. Electrode localization

Electrode localization was performed by coregistering Preimplantation magnetic resonance imaging and postimplantation computerized tomography axial images using LEAD-DBS software [45,46] and the electrode trajectories were mapped using iElectrodes software [47]. Eight brain regions were uniformly selected constituting the thalamo-cortical network, which is composed of amygdala (Amy),

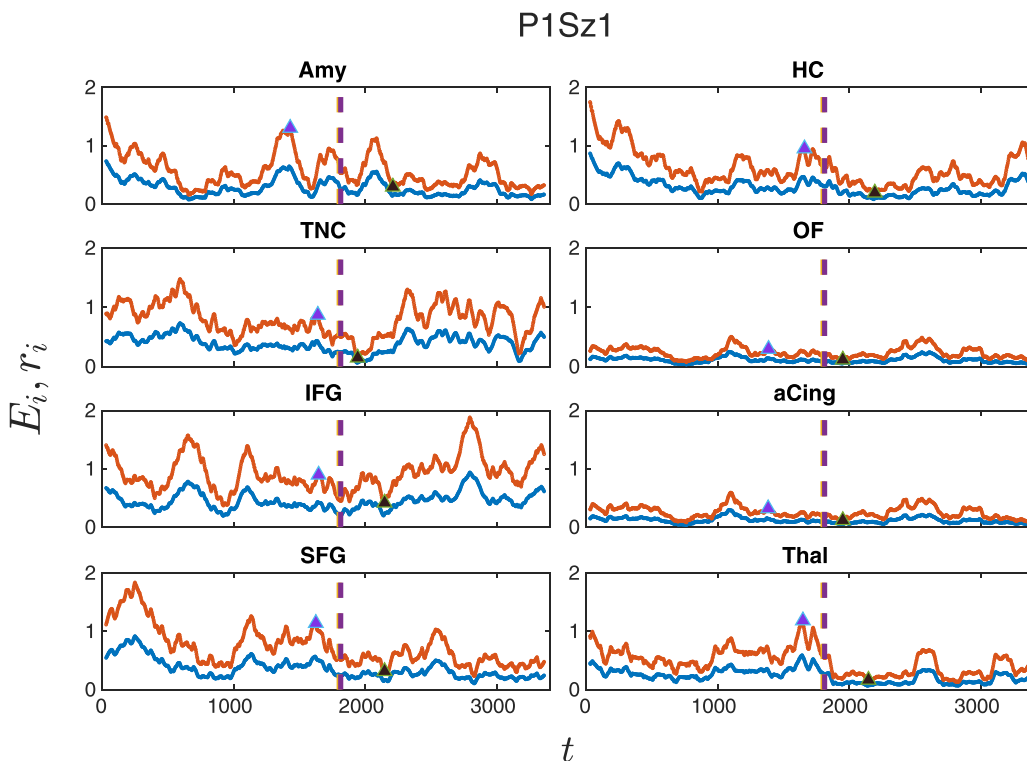


FIG. 8. Δ band for P1Sz1: The red and blue lines correspond to E_i vs time and r_i vs time, respectively, the yellow dashed line corresponds to the time where the ictal region starts, and the violet dashed line represents the end time where the ictal region ends.

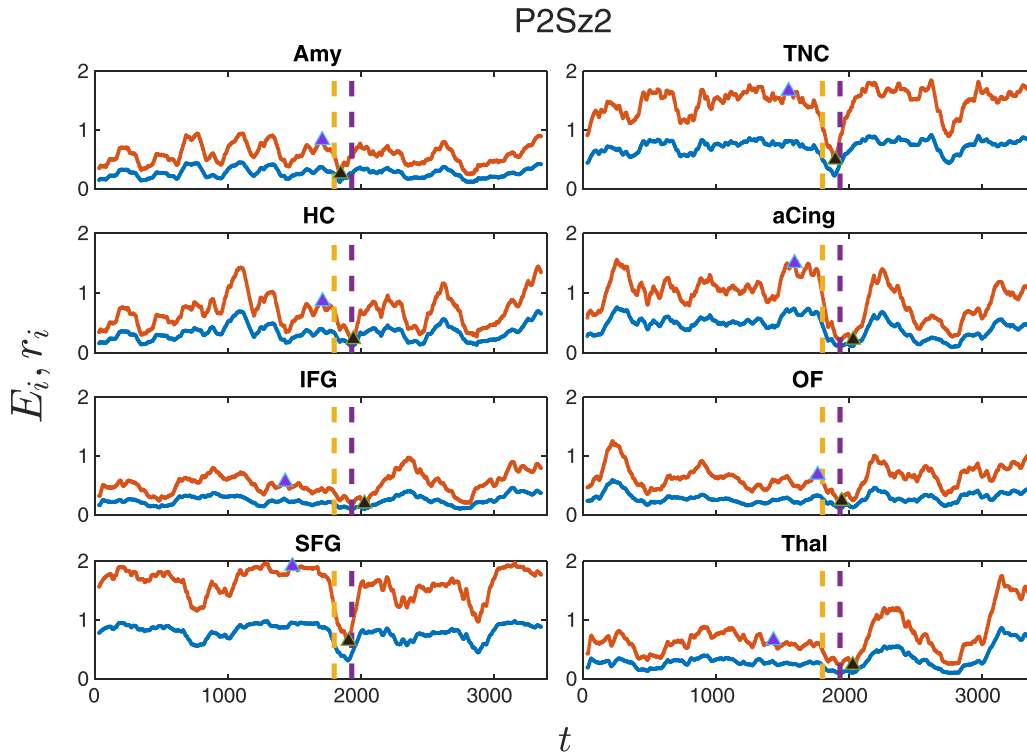


FIG. 9. Δ band for P2Sz2: The red and blue lines correspond to E_i vs time and r_i vs time respectively, the yellow dashed line represents the time where the ictal region starts, and the violet dashed line corresponds to the end time where the ictal region ends.

hippocampus (HC), temporal neocortex (TNC), superior and inferior frontal gyrus (S/I FG), anterior cingulate (aCing), orbitofrontal (OF), and thalamus (Thal). Moreover, as a representative of this global phenomenon we have sampled neural activity within the cortical (frontal, cingulate, lateral temporal) and subcortical (amygdala, hippo, and thalamus) regions. More importantly, these regions sampled are part of the limbic network that is involved in temporal lobe epilepsy and are commonly sampled for epilepsy surgery [48]. So these regions are functionally connected and are clinically relevant in epilepsy [49].

4. Data preprocessing and MVAR model

For each of the four seizures, the continuous SEEG data is composed of 30-min preictal, ictal, and 30-min postictal periods. The data were divided into 30-s epochs each with 3-s overlaps. The data were detrended and filtered by an eighth-order bandpass Butterworth filter with cutoff frequencies of 1–500 Hz. A multivariate autoregressive (MVAR) model $X(t) = \sum_{\tau=1}^p A(\tau)X(t - \tau) + \epsilon(t)$ of order ($p = 8$) was fit to each SEEG epoch from eight channels. The coefficients of the model, $A(\tau)$, were estimated using minimization of the residual noise $\epsilon(n)$ and were estimated via the Vieira-Morf partial correlation method. If the model fits the data well, the noise (innovation) vector $\epsilon(n) = [\epsilon_1(n), \dots, \epsilon_k(n)]^T$ follows a MV standard white noise process having zero mean and covariance matrix $\Sigma_e = \begin{pmatrix} \sigma_{11} & \dots & \sigma_{1K} \\ \vdots & \ddots & \vdots \\ \sigma_{K1} & \dots & \sigma_{KK} \end{pmatrix}$, assuming that each vector component is at least a weakly stationary time series. If we denote the $(K \times K)$ identity matrix as I_K , the

MVAR model can be transformed to the frequency domain, as $E(f) = B(f)y(f)$, where $E(F)$ is the Fourier transform of the residual noise vector and $B(f) = I_k - \sum_{\tau=1}^p A(\tau)e^{-j2\pi f\tau}$. Assuming that $\epsilon(n)$ is the input signal to the model and $y(n)$ the output signal from the model, $B(f)$ essentially results from the Fourier transform of the augmented matrix of the coefficients of the model [setting $A(0) = I_k$].

5. Directed functional connectivity measure

Partial directed coherence (PDC) was introduced by Baccala and Sameshima in 2001 as a normalized estimate between the interval $[0,1]$ and measures per frequency of the ratio of the outflow of the channel to channel i overall outflows from channel j [50]. PDC inherently distinguishes between direct and indirect interactions and can capture the directed and weighted Granger-connectivity structure scheme between each pair in the network. A generalized form of PDC (gPDC) was proposed by Baccala in 2007 which introduced a second inner normalization that makes it very robust with regard to inaccuracies and variability of measured data [51]. It is based on the Fourier transformed augmented coefficient matrix, $B_{ij}(f)$, and the diagonal elements of the covariance matrix, σ_{kk} , of the innovation process of the MVAR model, and is defined as

$$\text{gPDC}_{j \rightarrow i}(f) = \frac{|B_{ij}(f)|/\sigma_{ii}}{\sqrt{\sum_k |B_{kj}(f)|^2/\sigma_{kk}^2}}$$

gPDC is normalized between the interval $[0,1]$, as well.

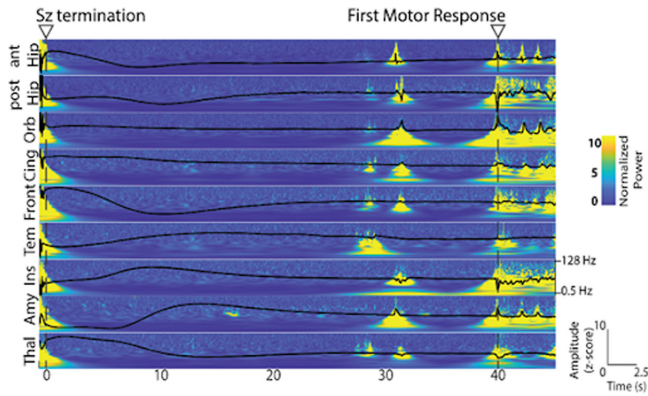


FIG. 10. Time-frequency representation from stereo EEG trace showing an absence of neural activity between 0 and 29 s of PGES. First motor response ($t = 40$ s) was preceded by a burst of neural activity at 30 s. Thal, centromedian thalamus; Amy, amygdala; Ins, insula; Tem, lateral temporal; Orb, orbitofrontal; Front, lateral frontal; ant and post hippocampus; cing-ant, cingulate; and PGES, postictal generalized EEG suppression.

APPENDIX C: SIMULATION RESULTS FOR OTHER PATIENTS

We have performed numerical simulations using dissimilar repulsive feedback coupled SL oscillators on networks obtained from two more seizure data (Figs. 8 and 9). The results show similar behavior to other seizures which helps us in proving the robustness of our findings.

APPENDIX D: PGES AND RELATION TO SUPPRESSION TO NEURAL ACTIVITY

PGES is a well-established electrophysiological phenomenon associated with an increased risk of SUDEP (sudden unexpected death in epilepsy). A landmark prospective multicenter study (called MORTEMUS) published in the prestigious journal *Lancet Neurology* confirmed the presence

of PGES in all the observed cases of SUDEP. PGES is defined as diffuse scalp EEG background suppression $< 10 \mu\text{V}$ observed postictally. The “G” in PGES represents spatial (“generalized or diffuse”) suppression observed in scalp EEG. Thus, during the PGES phenomenon, there is unequivocal generalized amplitude suppression as recorded by scalp EEG.

Examples of a few intracranial EEG studies during PGES are in Refs [52,53]. Similarly, over the last 5 years, we had collated and curated rare intracranial EEG (stereo EEG) data when patients had generalized tonic-clonic seizures followed by scalp EEG confirmed PGES. These patients had simultaneous scalp EEG and invasive stereo EEG recordings from multiple brain regions during epilepsy surgical evaluation. In addition, we recorded invasive EEG from thalamic subregions through Institutional Review Board (IRB)-approved protocol. Thus we have rare recordings from cortical and thalamic brain regions during scalp EEG confirmed PGES. To date, no center has reported human thalamocortical invasive EEG changes during PGES. Thus our data is novel and is uniquely poised to provide insights into thalamocortical changes during the scalp and invasive EEG-confirmed amplitude suppression (PGES).

During PGES, there is a diffuse scalp EEG suppression, and we have selected the cases where there is confirmed thalamocortical invasive EEG suppression (as in Fig. 10). This paper only used invasive stereo depth electrode recordings for signal processing and modeling. Further, we wish to highlight that for the signal processing, we have only used stereo depth electrode recordings. These recordings [also sometimes called local field potentials (LFPs)] from clinical depth electrodes are used in developing brain-computer interfaces (like language and motor mapping and modulation), seizure mapping, and subsequent surgical resection with the underlying *a priori* that bipolar montage-derived LFPs from invasive EEG electrodes have high signal fidelity and represent local neural ensemble activity [54]. During PGES, we have confirmed suppression of neural activity from direct invasive EEG recordings from the thalamocortical regions (like Fig. 10), and this data was used for modeling.

- [1] M. Kim, R. Roy, J. Aron, T. Carr, and I. Schwartz, Scaling Behavior of Laser Population Dynamics with Time-Delayed Coupling: Theory and Experiment, *Phys. Rev. Lett.* **94**, 088101 (2005).
- [2] G. Saxena, A. Prasad, and R. Ramaswamy, Amplitude death: The emergence of stationarity in coupled nonlinear systems, *Phys. Rep.* **521**, 205 (2012).
- [3] B. Gallego and P. Cessi, Decadal variability of two oceans and an atmosphere, *J. Climate* **14**, 2815 (2001).
- [4] T. Banerjee and D. Ghosh, Experimental observation of a transition from amplitude to oscillation death in coupled oscillators, *Phys. Rev. E* **89**, 062902 (2014).
- [5] A. Koseska, E. Volkov, and J. Kurths, Transition from Amplitude to Oscillation Death via Turing Bifurcation, *Phys. Rev. Lett.* **111**, 024103 (2013).
- [6] A. Koseska, E. Volkov, and J. Kurths, Oscillation quenching mechanisms: Amplitude vs. oscillation death, *Phys. Rep.* **531**, 173 (2013).
- [7] J. Wang and W. Zou, Collective behaviors of mean-field coupled Stuart–Landau limit-cycle oscillators under additional repulsive links, *Chaos* **31**, 073107 (2021).
- [8] T. Banerjee and D. Ghosh, Transition from amplitude to oscillation death under mean-field diffusive coupling, *Phys. Rev. E* **89**, 052912 (2014).
- [9] M. Nandan, C. Hens, P. Pal, and S. Dana, Transition from amplitude to oscillation death in a network of oscillators, *Chaos* **24**, 043103 (2014).
- [10] C. Hens, O. Olusola, P. Pal, and S. Dana, Oscillation death in diffusively coupled oscillators by local repulsive link, *Phys. Rev. E* **88**, 034902 (2013).
- [11] R. Karnatak, R. Ramaswamy, and A. Prasad, Amplitude death in the absence of time delays in identical coupled oscillators, *Phys. Rev. E* **76**, 035201 (2007).
- [12] Z. Hou and H. Xin, Oscillator death on small-world networks, *Phys. Rev. E* **68**, 055103 (2003).

- [13] L. Rubchinsky and M. Sushchik, Disorder can eliminate oscillator death, *Phys. Rev. E* **62**, 6440 (2000).
- [14] W. Liu, X. Wang, S. Guan, and C. Lai, Transition to amplitude death in scale-free networks, *New J. Phys.* **11**, 093016 (2009).
- [15] U. Verma, A. Sharma, N. Kamal, and M. Shrimali, First order transition to oscillation death through an environment, *Phys. Lett. A* **382**, 2122 (2018).
- [16] U. Verma, A. Sharma, N. Kamal, and M. Shrimali, Explosive death in complex network, *Chaos* **29**, 063127 (2019).
- [17] U. Verma and G. Ambika, Tipping induced by multiplexing on two-layer networks, *Eur. Phys. J.: Spec. Top.* **230**, 3299 (2021).
- [18] O. Maslennikov and V. Nekorkin, Hierarchical transitions in multiplex adaptive networks of oscillatory units, *Chaos* **28**, 121101 (2018).
- [19] E. O’Sullivan-Greene, I. Mareels, D. Freestone, L. Kulhmann, and A. Burkitt, A paradigm for epileptic seizure prediction using a coupled oscillator model of the brain, in *2009 Annual International Conference of the IEEE Engineering in Medicine and Biology Society (IEEE, 2009)*, pp. 6428–6431.
- [20] V. Grigorovsky, D. Jacobs, V. Breton, U. Tufa, C. Lucasius, J. Campo, Y. Chinvarun, P. Carlen, R. Wennberg, and B. Bardakjian, Delta-gamma phase-amplitude coupling as a biomarker of postictal generalized EEG suppression, *Brain Commun.* **2**, fcaa182 (2020).
- [21] P. Bauer, R. Thijs, R. Lamberts, D. Velis, G. Visser, E. Tolner, J. Sander, F. Silva, and S. Kalitzin, Dynamics of convulsive seizure termination and postictal generalized EEG suppression, *Brain* **140**, e18 (2017).
- [22] H. Kim, J. Y. Moon, G. A. Mashour, and U. Lee, Mechanisms of hysteresis in human brain networks during transitions of consciousness and unconsciousness: Theoretical principles and empirical evidence, *PLoS Comput. Biol.* **14**, e1006424 (2018).
- [23] A. L. Hodgkin, and A. F. Huxley, Propagation of electrical signals along giant nerve fibres, *Philos. Trans. R. Soc., B* **140**, 177 (1952).
- [24] R. FitzHugh, Impulses and physiological states in theoretical models of nerve membrane, *Biophys. J.* **1**, 445 (1961).
- [25] J. L. Hindmarsh and R. M. Rose, A model of neuronal bursting using three coupled first order differential equations, *Proc. R. Soc. London, Ser. B* **221**, 87 (1984).
- [26] M. Breakspear, Dynamic models of large-scale brain activity, *Nat. Neurosci.* **20**, 340 (2017).
- [27] A. Pathak, D. Roy, and A. Banerjee, Whole-brain network models: From physics to bedside, *Front. Comput. Neurosci.* **16**, 866517 (2022).
- [28] M. Breakspear, S. Heitmann, and A. Daffertshofer, Generative models of cortical oscillations: neurobiological implications of the Kuramoto model, *Front. Hum. Neurosci.* **4**, 190 (2010).
- [29] M. Demirtaş, C. Falcon, A. Tucholka, J. D. Gispert, J. L. Molinuevo, and G. Deco, A whole-brain computational modeling approach to explain the alterations in resting-state functional connectivity during progression of Alzheimer’s disease, *NeuroImage: Clinical* **16**, 343 (2017).
- [30] A. López-González, R. Panda, A. Ponce-Alvarez, G. Zamora-López, A. Escrichs, and C. Martial, Loss of consciousness reduces the stability of brain hubs and the heterogeneity of brain dynamics, *Commun. Biol.* **4**, 1 (2021).
- [31] R. Mirollo and S. Strogatz, Amplitude death in an array of limit-cycle oscillators, *J. Stat. Phys.* **60**, 245 (1990).
- [32] M. Frasca, A. Bergner, J. Kurths, and L. Fortuna, Bifurcations in a star-like network of Stuart-Landau oscillators, *Int. J. Bifurcation Chaos* **22**, 1250173 (2012).
- [33] R. Albert and A. Barabási, “Statistical mechanics of complex networks,” *Rev. Mod. Phys.* **74**, 47 (2002).
- [34] B. Ermentrout, XPPAUT, *Computational Systems Neurobiology* (Springer, New York, 2012), pp. 519–531.
- [35] M. Asadollahi, M. Noorbakhsh, L. Simani, M. Ramezani, and K. Gharagozli, Two predictors of postictal generalized EEG suppression: Tonic phase duration and postictal immobility period, *Seizure* **61**, 135 (2018).
- [36] S. Lhatoo, H. Faulkner, K. Dembny, K. Trippick, C. Johnson, and J. Bird, An electroclinical case-control study of sudden unexpected death in epilepsy, *Ann. Neurol.* **68**, 787 (2010).
- [37] M. Seyal, K. Hardin, and L. Bateman, Postictal generalized EEG suppression is linked to seizure-associated respiratory dysfunction but not postictal apnea, *Epilepsia* **54**, 377 (2013).
- [38] K. Kanth, C. Zimmerman, S. Toprani, and M. Seyal, Duration of postictal impaired awareness after bilateral tonic-clonic seizures: EEG and patient characteristics, *Epilepsy Behav.* **128**, 108576 (2022).
- [39] I. Aiba, and J. L. Noebels, Spreading depolarization in the brainstem mediates sudden cardiorespiratory arrest in mouse SUDEP models, *Sci. Transl. Med.* **7**, 282ra46 (2015).
- [40] S. Jalan and C. Sarkar, Complex networks: An emerging branch of science, *Phys. News* **47**, 3 (2017).
- [41] A. D. Kachhvah and S. Jalan, Hebbian plasticity rules abrupt desynchronization in pure simplicial complexes, *New J. Phys.* **24**, 052002 (2022).
- [42] A. D. Kachhvah and S. Jalan, First-order route to antiphase clustering in adaptive simplicial complexes, *Phys. Rev. E* **105**, L062203 (2022).
- [43] E. Toth, S.S.Kumar, G. Chaitanya, K. Riley, K. Balasubramanian, and S. Pati, Reliable detection of focal-onset seizures in the human anterior nucleus of the thalamus using non-linear machine learning, *medRxiv* (2020), doi: 10.1101/2020.09.18.20196857.
- [44] G. Chaitanya, A. Romeo, A. Ilyas, A. Irannejad, E. Toth, G. Elsayed, J. Bentley, K. Riley, and S. Pati, Robot-assisted stereoelectroencephalography exploration of the limbic thalamus in human focal epilepsy: Implantation technique and complications in the first 24 patients, *Neurosurg. Focus* **48**, E2 (2020).
- [45] A. Horn and A. Kühn, Lead-DBS: A toolbox for deep brain stimulation electrode localizations and visualizations, *NeuroImage* **107**, 127 (2015).
- [46] www.lead-dbs.org
- [47] A. Blenkmann, H. Phillips, J. Princich, J. Rowe, T. Bekinschtein, C. Muravchik, and S. Kochen, Ielectrodes: A comprehensive open-source toolbox for depth and subdural grid electrode localization, *Front. Neuroinf.* **11**, 14 (2017).
- [48] V. RajMohand and E. Mohandas, The limbic system, *Indian J. Psychiatry* **49**, 132 (2007).
- [49] L. Bonilha, T. Nesland, G. U. Martz, J. E. Joseph, M. V. Spampinato, J. C. Edwards, and A. Tabesh, Medial temporal lobe epilepsy is associated with neuronal fibre loss and paradoxical increase in structural connectivity of limbic structures, *J. Neurol., Neurosurg., Psychiatry* **83**, 903 (2012).

- [50] L. A. Baccalá and K. Sameshima, Partial directed coherence: A new concept in neural structure determination, *Biol. Cybern.* **84**, 463 (2001).
- [51] L. Baccala, K. Sameshima, and D. Takahashi, Generalized partial directed coherence, in *2007 15th International Conference on Digital Signal Processing (DSP 2007)* (IEEE, 2007), pp. 163-166.
- [52] A. Marchi, B. Giusiano, M. King, S. Lagarde, A. Trébuchon-Dafonseca, C. Bernard, S. Rheims, F. Bartolomei, and A. McGonigal, Postictal electroencephalographic (EEG) suppression: A stereo-EEG study of 100 focal to bilateral tonic-clonic seizures, *Epilepsia* **60**, 63 (2019).
- [53] L. M. Bateman, A. Mendiratta, J. Y. Liou, E. J. Smith, C. W. Bazil, H. Choi, G. M. McKhann, A. Pack, S. Srinivasan, and C. A. Schevon, Postictal clinical and electroencephalographic activity following intracranially recorded bilateral tonic-clonic seizures, *Epilepsia* **60**, 74 (2019).
- [54] A. Dubey and S. Ray, Cortical electrocorticogram (ECoG) is a local signal, *J. Neurosci.* **39**, 4299 (2019);